Nanoscale

PAPER

Cite this: *Nanoscale*, 2022, **14**, 17460

Durable Cu_xO/mesoporous TiO_2 photocatalyst for stable and efficient hydrogen evolution†

Lingling Cui,‡[a] Chunyao Niu, ‡[b] Young Soo Kang,[c] Rachel A. Caruso[d] and Xiao Li Zhang *[a]

Received 8th August 2022,
Accepted 14th November 2022

DOI: 10.1039/d2nr04343b

rsc.li/nanoscale

Heterogeneous structures containing highly dispersed semiconductor nanoparticles on a photoactive support are effective for the photocatalytic hydrogen evolution reaction (HER). In this work, the interlayer ion-exchange and space confining nature of layered titanate nanosheets was used to embed copper ions in titanates, which were then transitioned to mesoporous Cu_xO/TiO_2 with highly dispersed Cu_xO nanostructures. Both experimental and density functional theory (DFT) studies demonstrated that the fine-decoration of Cu_xO nanostructures and the reducible valence of the copper species enabled stable superior photocatalytic activity. The HER efficiency was enhanced to 12.45 mmol g^{-1} h^{-1} for the mesoporous Cu_xO/TiO_2 composites in comparison to an efficiency of 0.38 mmol g^{-1} h^{-1} for the non-modified TiO_2. Steady HER performances over 10 h, cyclic HER measurement over 60 h, and testing of the composite kept under ambient conditions for over one year, demonstrated excellent stability of the composite against photochemical and wet-chemical erosion.

Introduction

Hydrogen is an ideal alternative to fossil fuels because it can be produced with zero carbon emissions, it has a high energy density and is light weight.[1–3] Effective harnessing of sunlight provides an opportunity to realize a sustainable hydrogen economy through efficient photocatalytic hydrogen generation.[4–9] The current benchmark heterogeneous photocatalysts utilize noble metals (Au, Pt, and Ag) to achieve well-aligned local work functions and electronic structures for rapid charge separation and transfer, as well as durability against corrosion.[10–15] Insufficient reserves and significant cost, however, hamper the use of noble metals for commercial-scale sustainable hydrogen production. Development of low-cost, earth abundant alternatives with comparable HER photocatalytic activity and stability is of strategic interest towards a future hydrogen economy.[8,16]

Titanium dioxide and copper oxides are abundant natural resources, that are environmentally benign, low-cost, with inherent activity and durability that make them ideal candidates for transition metal based heterogeneous photocatalysts.[17–23] To date, the most feasible synthesis approaches for large-scale preparation, *e.g.*, impregnation or co-precipitation, have demonstrated some success in control over particle size. However, the commonly recognized challenges to inhibit particle agglomeration and growth during the HER have been drawbacks for maintaining stable photocatalytic activity.[24–26]

Making use of the intrinsic ion-exchangeable nature and the interlayer space confinement of sodium titanate, the present work demonstrates a facile confined synthesis of highly dispersed Cu_xO nanostructures decorated on mesoporous TiO_2 spheres. The porous properties of these structures were beneficial for photocatalytic HER as they allowed efficient transport of the reactive species, while the reducible oxidation state of the copper species improved band alignment for rapid charge transfer. The Cu_xO/TiO_2 composites demonstrated superior photocatalytic HER efficiency of 12.45 mmol g^{-1} h^{-1} during 12 HER cycles (over 60 h) and excellent durability. The oxidation states of the copper species also allowed the composites to be kept under ambient conditions for over one year without activity decay. In comparison to other confined methods relying on hard or soft templates, *e.g.* MOF or SiO_2, the interlayer confinement strategy offers a much simpler and more cost-effective approach with mild environmental impact for practical applications.

[a]*School of Materials Science and Engineering, Zhengzhou University, 450001 P.R. China. E-mail: xiaolizhang.z@gmail.com*
[b]*School of Physics and Microelectronics, Zhengzhou University, 450001 P.R. China*
[c]*Environmental and Climate Technology, Korea Institute of Energy Technology (KENTECH), 200 Hyeoksin-ro, Naju City, Jeollanamdo 58330, Korea*
[d]*Applied Chemistry and Environmental Science, School of Science, RMIT University, Melbourne, VIC 3001, Australia*

†Electronic supplementary information (ESI) available. See DOI: **https://doi.org/10.1039/d2nr04343b**

‡Equal contribution.

Results and discussion

The process for incorporating the copper ions in the titanate nanosheet spherical structures is depicted in Scheme 1, with full details given in the ESI.† The sodium ions are partially removed by hydrogen through initially protonation using hydrochloric acid solution. Copper ions are embedded into the nanosheets through ion-exchange with the remaining sodium ions when soaking the samples in a concentrated Cu(II) acetate solution. The extent of protonation can be altered by changing the hydrochloric acid concentration, thus varying the residual sodium ions that can be ion-exchanged for Cu(II) ions. Five samples were prepared from the samples with increasing HCl concentrations (0.05, 0.10, 0.15, 0.20 and 0.25 M HCl) during the protonation step and were labelled as CT1 precursor–CT5 precursor. This process enabled a tuneable copper content in the final Cu_xO/TiO_2 composites that were obtained following calcination at 450 °C (labelled CT1–CT5). The heating of the samples alters the morphological structure within the spheres, as discussed later.

The copper titanate microspheres are greater than a micrometre in diameter (see Transmission Electron Microscopy (TEM) image of the CT1 precursor in Fig. 1a and appear to be composed of nanosheets, as seen in the higher magnification TEM images of the microsphere surface in Fig. 1b and c. Elemental analyses show a relatively homogeneous distribution of both Ti and Cu across the spheres, see Fig. 1d–f. Using inductively coupled plasma-optical emission spectroscopy (ICP-OES), the copper content of the final mesoporous Cu_xO/TiO_2 composites was obtained, as listed in Table S1.† The copper content decreased from 8.6 wt% (CT1) to 3.9 wt% (CT5) as acid of higher concentration was used in the synthesis. This led to a colour change from dark brownish green (CT1) to light green (CT5) as shown in the optical images in Fig. S1.†

Calcination induced decomposition and structural deformation of the Cu/titanate sheets led to the formation of small copper oxide nanostructures decorated on the TiO_2 mesoporous spheres, as displayed in images from CT3, Fig. 2a and e. Fig. 2b–d show the elemental line scan and mapping analyses, demonstrating evenly distributed Ti and Cu across the structure. The high resolution-TEM (HR-TEM) image in Fig. 2f and g reveal lattice spacing of 0.35 nm, attributed to the anatase TiO_2 (101) plane,[17] and lattice spacing of 0.25 nm, corresponding to either the (002) plane of CuO[27] or the (111) plane of Cu_2O.[28] Fig. 2h shows a typical type IV N_2 sorption isotherm with hysteresis that indicates a mesoporous structure with a pore size distribution centred at 17 nm (see inset). The Brunauer, Emmett, Teller (BET) specific surface area was 187.6 $m^2\ g^{-1}$ for CT3.

The XPS spectrum of CT3 exhibits two dominant peaks for Ti $2p_{3/2}$ and Ti $2p_{1/2}$ of the Ti^{4+} at 458.3 eV and 464.2 eV, and two weak shoulder peaks for Ti $2p_{3/2}$ and $2p_{1/2}$ of the Ti^{3+} at

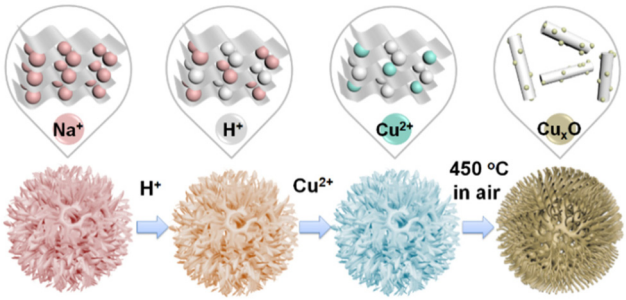

Scheme 1 Schematic illustrating the preparation of the mesoporous Cu_xO/TiO_2 composites. First sodium titanate is partially protonated in HCl solution, then ion-exchanged with Cu(II) followed by calcination in air.

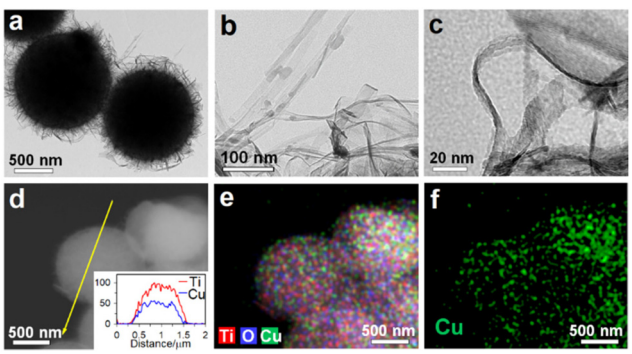

Fig. 1 (a–c) TEM images and (d–f) elemental analyses, including (d) and inset showing a line scan analysis; (e) elemental mapping image; and (f) Cu mapping of the copper titanate spheres (CT1 precursor).

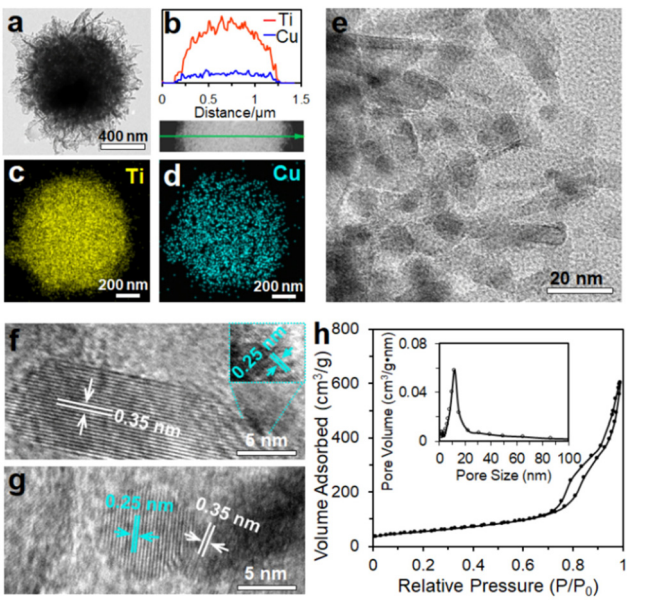

Fig. 2 (a) TEM image of spherical structure, (b) line scan elemental analyses, (c) and (d) element mapping for Ti and Cu, respectively; (e) TEM image of the particles at the surface of the sphere; (f and g) HR-TEM images; (h) nitrogen sorption isotherm with pore size distribution (inset) of the mesoporous Cu_xO/TiO_2 composite, CT3.

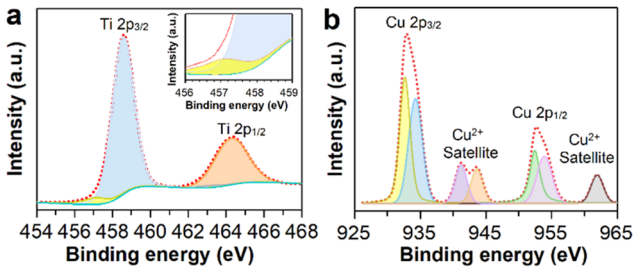

Fig. 3 XPS spectra of (a) Ti 2p (inset higher magnification, between 456–459 eV) and (b) Cu 2p of the mesoporous Cu_xO/TiO_2 composite, CT3.

457.0 eV and 461.8 eV, respectively Fig. 3.[29] The existence of Ti^{3+} is generally considered beneficial in photocatalytic application for retarding the charge recombination and thus enhancing the photocatalytic efficiency.[30,31] The XPS spectrum in Fig. 3b reveals a Cu 2p peak consisting of a typical pair of characteristic binding energies at 934.0 and 953.9 eV that can be attributed to the Cu $2p_{3/2}$ and Cu $2p_{1/2}$ of Cu^{2+} with two satellite single peaks at 941.2 and 943.6 eV.[32,33] Binding energies for Cu $2p_{3/2}$ (932.6 eV) and Cu $2p_{1/2}$ (952.4 eV) indicate the coexistence of Cu^+ and Cu^{2+} in the Cu_xO/TiO_2 composite with a Cu(I)/Cu(II) ratio of approximately 1.06.[34–36] A gradual decrease in the Ti^{3+} and Cu^{2+} peaks is observed in the XPS spectra for the mesoporous Cu_xO/TiO_2 composites (CT1–CT5), Fig. S2,† as the copper content is reduced.

The XRD patterns of the mesoporous Cu_xO/TiO_2 composites and mesoporous TiO_2, Fig. 4a and Fig. S3a,† respectively, are dominated by the major diffraction peaks of anatase TiO_2 (JCPDS card no. 71-1166) with peaks at 2θ of 25.2°, 37.8°, and 48.1° representing the (101), (004), and (200) planes, respectively.[23] No clear peak for copper oxide can be observed, even at high copper contents, when focusing in on the enlarged area of the XRD, Fig. 4b. The Raman spectra of the mesoporous Cu_xO/TiO_2 composites, in Fig. 4c, include four characteristic peaks at 143, 399, 516, and 640 cm^{-1} that can be ascribed to anatase.[37] The peak at 143 cm^{-1} slightly shifted from 143.7 cm^{-1} for CT1–CT3 to 141.9 cm^{-1} for CT4 and CT5 with a slightly decreased FWHM from 20 cm^{-1} to 18 cm^{-1}, which is attributed to a decrease in the surface strain as the copper loading decreases.[36,38] In Fig. 4d, the broad absorbance from 360–550 nm in the UV-vis spectra of the Cu_xO/TiO_2 composites can be attributed to Cu_xO.[1,39] The gradual decrease in absorbance between 400–500 can be assigned to the interfacial electron transfer from the valence band of TiO_2 to the conduction bands of Cu_xO.[40] The d–d transition of Cu^{2+} and the intrinsic exciton band of CuO induced the absorbance in the long wavelength region (600–800 nm).[21,40–42] The absorbance at the rage of 500–600 nm can be attributed to the interband absorption of Cu_2O.[42]

Photocatalytic HER activities of the composites were measured in a 20 vol% methanol aqueous solution (Fig. 5). Without Cu_xO present, the TiO_2 mesoporous spheres (control sample T) achieved a HER rate slightly better than that of commercial P25 TiO_2 nanoparticles (referred to as P25), as shown in Fig. 5a. In contrast, the mesoporous Cu_xO/TiO_2 composites exhibited significantly enhanced HER rates, reaching a maximum of 12.45 mmol g^{-1} h^{-1} for CT3 then decreasing again as the copper content decreased in the samples. This suggests the finely dispersed Cu_xO nanostructure plays an important role in determining the photocatalytic HER performance, with the benefit increasing initially with copper loading and then decreasing when the copper loading was

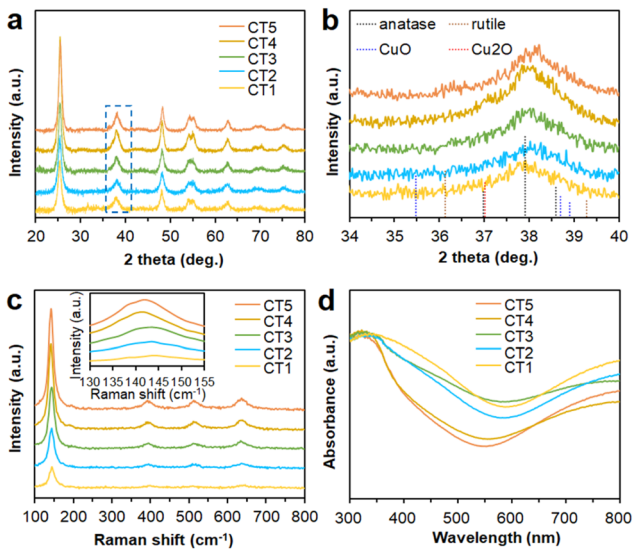

Fig. 4 (a) XRD patterns; (b) enlarged XRD patterns between 2θ of 34° to 40°; (c) Raman spectra, inset showing peak between 130 and 155 cm^{-1}; and (d) UV-vis absorbance spectra of the Cu_xO/TiO_2 composites, CT1–CT5.

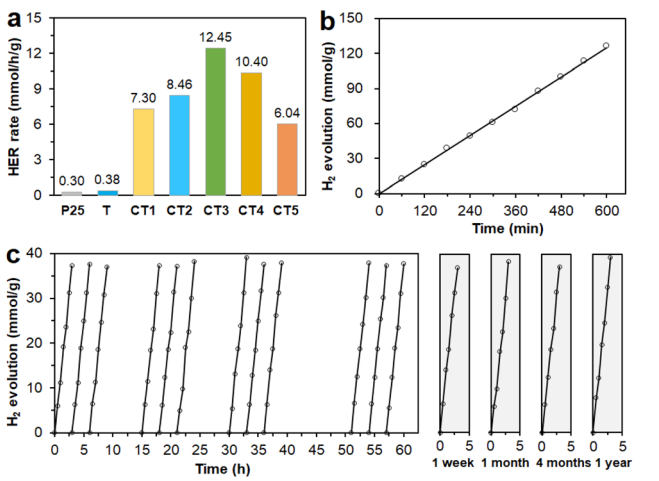

Fig. 5 (a) HER rates for P25, TiO_2 mesoporous spheres (T) and the mesoporous Cu_xO/TiO_2 composites; (b) hydrogen evolution over 10 h for CT3; and (c) cyclic HER (12 cycles over 60 h), along with a durability test run intermittently with the sample left under ambient conditions over 1 year for CT3. All experiments were carried out after pre-illumination for 45 min.

>6.8 wt%. Apparent quantum efficiency (AQE) for the HER of the CT3 was approximately 2.51% at a wavelength of 350 nm.

The stability of the CT3 was investigated for photocatalytic HER performance by conducting 12 cyclic HER measurements and also running tests intermittently (at 1 week, 1 month, 4 months and 1 year) with a sample left under ambient conditions over one year. The CT3 sample exhibited a stable HER rate during the 10 h single measurement (Fig. 5b) and consistent performance during cyclic reactions for 12 cycles over 60 h with no activity decline (Fig. 5c). The HER performance of the CT3 kept under ambient conditions at one week, one month, four months and one year demonstrated the excellent long-term stability of the CT3 sample. The best HER rate was 15.94 mmol g^{-1} h^{-1} during the stability testing. Compared with copper oxide-based TiO_2 composites that have been reported in the literature, see Table S2,† CT3 exhibited superior stability for HER.

For comparison, Cu_xO/TiO_2 composites based on commercial P25 TiO_2 nanoparticles were prepared through conventional impregnation to have the same copper loading as the CT1–5 samples. The Cu_xO/P25 TiO_2 composites were darker in colour than the mesoporous Cu_xO/TiO_2 composites (Fig. S4†). As displayed in Fig. S5,† the P25 TiO_2 based composites reached 18–33% of the HER rates that the mesoporous Cu_xO/TiO_2 with the same copper content achieved. Of these samples, P3, with 6.8 wt% copper, has the best HER rate of 3.03 mmol g^{-1} h^{-1}, which is a quarter of the HER rate of the mesoporous CT3 sample.

The influence of particle size and specific surface area were also investigated by increasing the calcination temperature to 500 °C for CT3 (denoted as CT3-500). A dramatic drop in the HER rate of approximately 26% was seen for the CT3-500 sample, Fig. S6.† XRD analysis of CT3-500, Fig. S7a,† reveals the characteristic peak of CuO, indicating the presence of a significantly increased CuO particle size in the composite that had been calcined at higher temperature. Fig. S7b and c† show a TEM image and the elemental mapping analyses of the CT3-500 where large Cu_xO agglomerates can be observed. From the gas sorption data, Fig. S5d,† the BET surface area of CT3-500 was calculated to be 104.8 m^2 g^{-1}, which indicates a dramatic drop from the CT3 (187.6 m^2 g^{-1}), and a pore size centred at 19 nm, Fig. S5e.† Both the high surface area of the composite and the small Cu_xO size are expected to contribute to the higher HER rate for CT3 compared to CT3-500.

Although strong visible light absorbance for the mesoporous Cu_xO/TiO_2 composites (Fig. 4d), no HER activity was observed with visible light illumination (>420 nm). Thus, indicating that photoexcitation occurs within TiO_2 and the electron transfers from the TiO_2 to the Cu_xO. This was confirmed by the significant fluorescence quenching seen in the photoluminescence spectra of CT3 in comparison to the pure TiO_2 (T), Fig. 6a, indicating less recombination in the Cu_xO/TiO_2 composite than the TiO_2. Fig. 6b displays the photocatalytic HER activity as a function of the illumination time where rapid activity development was observed during the first 45 min after which it became relatively constant.

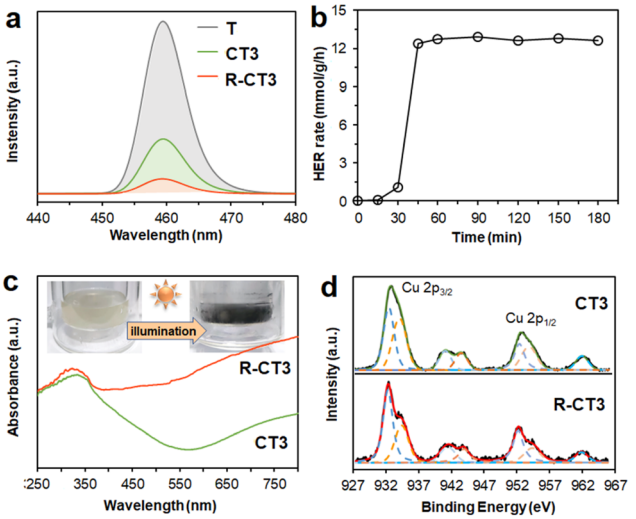

Fig. 6 (a) Photoluminescence spectra of TiO_2, CT3 and R-CT3 in 20 vol% methanol aqueous solution; (b) HER rate of CT3 as a function of illumination time; (c) UV-vis absorbance spectra and optical observations (inset), and (d) XPS analyses of Cu 2p of CT3 and R-CT3.

The heterogeneous photocatalyst was retrieved (R-CT3) after 180 min of the HER and analysed. Following this activation, there was a further decrease in photoluminescence for the R-CT3, Fig. 6a, indicating improved photoexcited electron transfer from the conduction band of TiO_2 to the Cu_xO after illumination. The reaction solution also gradually changed colour from light brown to black in the first 45 minutes of illumination, Fig. 6c. UV-vis absorbance of the R-CT3 exhibited strong absorbance over the 400–800 nm wavelength range, especially, the interband absorption of Cu_2O induced absorbance between 500–600 nm.[40] XPS analyses, Fig. 6d, show an increase in the Cu(I)/Cu(II) ratio from approximately 1.06 for the CT3 to 1.66 for the retrieved CT3 (R-CT3). This result suggests that reduction of Cu^{2+} to Cu^{+} occurred under illumination, driven by electron injection into the Cu_xO from the conduction band of TiO_2. The change in oxidation state of the copper oxide alters the heterojunction properties, which enhances the photocatalytic HER activity that was accompanied with the colour change of photocatalyst from light brown to black.

For an insight into the underlying mechanisms, density functional theory (DFT) was used to investigate the HER activity for the surfaces of TiO_2, CuO, and Cu_2O through evaluation of the hydrogen adsorption free energy ΔG_H. With an optimal value of 0 eV, ΔG_H is generally used to describe the activation energy of HER, which has demonstrated successful theoretical prediction for many different material systems.[43–45] The corresponding simulation is summarized in detail in the ESI.† The most stable low energy surface (111) of CuO and Cu_2O was used for the Cu_xO (Fig. 7a),[46] and the predominant (101)-facet for the TiO_2 was used (Fig. S8†). For the basal (101) surface of TiO_2, ΔG_H is approximately 0.6 eV uphill, as shown in Fig. 7b, suggesting low HER activity. With a strong endothermic ΔG_H of −1.21 eV, the strong bond between the

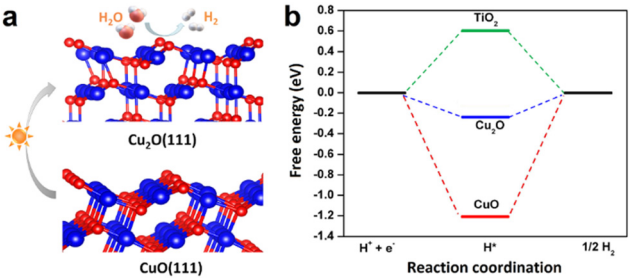

Fig. 7 (a) Schematic of Cu_2O (111) and CuO (111) surfaces, and the reduction from CuO to Cu_2O that prompted HER. Cu, O and H atoms are denoted with blue, red, and silver spheres, respectively. (b) The free energy *versus* the reaction coordinate of HER for the TiO_2 (101), CuO (111) and Cu_2O (111) systems.

(111) surface of CuO and the adsorbed H atoms makes it almost inert for the HER. In contrast, ΔG_H of the (111) plane of Cu_2O lies at around −0.24 eV, a far more optimal position for HER reaction than that of TiO_2 (101) surface and the CuO (111) surface. The results well agree with the aforementioned experimental findings, particularly, the HER enhancement from the change in oxidation state of the CuO.

Under illumination, the photoinduced electron might further reduce Cu^+ to Cu on the Cu_2O surface and temporarily form Cu_2O supported Cu clusters. The high activity of Cu cluster makes it easily reverse back to the oxidation state once without the illumination. To evaluate the influence from small metallic Cu cluster, Cu_{10} cluster was used to estimate ΔG_H of the Cu cluster on the Cu_2O (111) surface. Fig. S9,† the simulated ΔG_H of various Cu_{10} sites has an average value close to that of the Cu_2O (111) surface (−0.24 eV), which indicates similar HER activity of Cu_2O (111) and Cu_{10}@Cu_2O (111) systems.

Conclusions

In this work, an effective photocatalyst consisting of Cu_xO nanostructures decorated on mesoporous TiO_2 spheres was prepared through a simple confined synthesis that harnessed the interlayer ion-exchangeable and space confinement nature of titanate nanosheets. The obtained Cu_xO/TiO_2 photocatalysts demonstrated a photocatalytic HER efficiency of 12.45 mmol g^{-1} h^{-1} with excellent stability during a 12-cycle test over 60 h and prolonged storage under ambient conditions over one year. The highly dispersed Cu_xO nanostructures, large specific surface area and mesoporosity of the composite, as well as the reducible oxidation state of the copper species produced a system with excellent photoactivity and long-term stability.

Author contributions

All authors have contributed to the preparation of the manuscript and given approval to the final version of the manuscript.

Conflicts of interest

There are no conflicts to declare.

Acknowledgements

XLZ appreciates the support from National Natural Science Foundation of China (NSFC, Grant No.: 51602291). RAC acknowledges the Australian Research Council Discovery Project Scheme (DP180103815). CN acknowledges the Henan provincial key science and technology research project (No. 222102240023). YSK acknowledges the National Research Foundation of Korea (No. 2020R1A3B3079715).

References

1 T. Hisatomi and K. Domen, *Nat. Catal.*, 2019, **2**, 387–399.
2 T. He, P. Pachfule, H. Wu, Q. Xu and P. Chen, *Nat. Rev. Mater.*, 2016, **1**, 16059.
3 J. Zhu, L. Hu, P. Zhao, L. Y. S. Lee and K.-Y. Wong, *Chem. Rev.*, 2020, **120**, 851–918.
4 J. Ran, J. Zhang, J. Yu, M. Jaroniec and S. Z. Qiao, *Chem. Soc. Rev.*, 2014, **43**, 7787–7812.
5 Q. Wang and K. Domen, *Chem. Rev.*, 2020, **120**, 919–985.
6 Y. Wang, H. Suzuki, J. Xie, O. Tomita, D. J. Martin, M. Higashi, D. Kong, R. Abe and J. Tang, *Chem. Rev.*, 2018, **118**, 5201–5241.
7 S. Chen, T. Takata and K. Domen, *Nat. Rev. Mater.*, 2017, **2**, 17050.
8 G. D. Moon, J. B. Joo, I. Lee and Y. Yin, *Nanoscale*, 2014, **6**, 12002–12008.
9 R. Ye, J. Zhao, B. B. Wickemeyer, F. D. Toste and G. A. Somorjai, *Nat. Catal.*, 2018, **1**, 318–325.
10 P. Dong, Y. Wang, A. Zhang, T. Cheng, X. Xi and J. Zhang, *ACS Catal.*, 2021, **11**, 13266–13279.
11 S. Fang, Y. Liu, Z. Sun, J. Lang, C. Bao and Y. H. Hu, *Appl. Catal., B*, 2020, **278**, 119316.
12 Y. Deng, Z. Zhang, P. Du, X. Ning, Y. Wang, D. Zhang, J. Liu, S. Zhang and X. Lu, *Angew. Chem., Int. Ed.*, 2020, **59**, 6082–6089.
13 S. Wang, Z. J. Zhao, X. Chang, J. Zhao, H. Tian, C. Yang, M. Li, Q. Fu, R. Mu and J. Gong, *Angew. Chem., Int. Ed.*, 2019, **58**, 7668–7672.
14 L. Liu, M. Lopez-Haro, C. W. Lopes, C. Li, P. Concepcion, L. Simonelli, J. J. Calvino and A. Corma, *Nat. Mater.*, 2019, **18**, 866–873.
15 T. Wang, X. Tao, X. Li, K. Zhang, S. Liu and B. Li, *Small*, 2020, **17**, 2006255.
16 M. Xiao, L. Zhang, B. Luo, M. Lyu, Z. Wang, H. Huang, S. Wang, A. Du and L. Wang, *Angew. Chem., Int. Ed.*, 2020, **59**, 7230–7234.
17 Y. Zhang, J. Zhao, H. Wang, B. Xiao, W. Zhang, X. Zhao, T. Lv, M. Thangamuthu, J. Zhang, Y. Guo, J. Ma, L. Lin, J. Tang, R. Huang and Q. Liu, *Nat. Commun.*, 2022, **13**, 58.

18 B. H. Lee, S. Park, M. Kim, A. K. Sinha, S. C. Lee, E. Jung, W. J. Chang, K. S. Lee, J. H. Kim, S. P. Cho, H. Kim, K. T. Nam and T. Hyeon, *Nat. Mater.*, 2019, **18**, 620–626.

19 T. Wei, Y.-N. Zhu, X. An, L.-M. Liu, X. Cao, H. Liu and J. Qu, *ACS Catal.*, 2019, **9**, 8346–8354.

20 C. Cheng, W. H. Fang, R. Long and O. V. Prezhdo, *JACS Au*, 2021, **1**, 550–559.

21 Q. Shi, G. Ping, X. Wang, H. Xu, J. Li, J. Cui, H. Abroshan, H. Ding and G. Li, *J. Mater. Chem. A*, 2019, **7**, 2253–2260.

22 Y. Yuan, L. Sun, H. Gao, S. Mo, T. Xu, L. Yang and W.-W. Zhan, *Inorg. Chem.*, 2020, **59**, 16010–16015.

23 L. Cui, Y. Xu, J. Fan, P. Yuan, C. Sun, Z. Guo, X. L. Zhang and R. A. Caruso, *ACS Appl. Energy Mater.*, 2021, **4**, 4050–4058.

24 W. Kurashige, Y. Mori, S. Ozaki, M. Kawachi, S. Hossain, T. Kawawaki, C. J. Shearer, A. Iwase, G. F. Metha, S. Yamazoe, A. Kudo and Y. Negishi, *Angew. Chem., Int. Ed.*, 2020, **59**, 7076–7082.

25 R. van den Berg, T. E. Parmentier, C. F. Elkjær, C. J. Gommes, J. Sehested, S. Helveg, P. E. de Jongh and K. P. de Jong, *ACS Catal.*, 2015, **5**, 4439–4448.

26 W. Kurashige, R. Kumazawa, D. Ishii, R. Hayashi, Y. Niihori, S. Hossain, L. V. Nair, T. Takayama, A. Iwase, S. Yamazoe, T. Tsukuda, A. Kudo and Y. Negishi, *J. Phys. Chem. C*, 2018, **122**, 13669–13681.

27 S. Sharma, M. R. Pai, G. Kaur, Divya, V. R. Satsangi, S. Dass and R. Shrivastav, *Renewable Energy*, 2019, **136**, 1202–1216.

28 K. Yang, G. Cheng, R. Chen, K. Zhao, Y. Liang, W. Li and C. Han, *Energy Technol.*, 2021, 2100259.

29 H. Wei, E. F. Rodriguez, A. S. Best, A. F. Hollenkamp, D. Chen and R. A. Caruso, *Adv. Energy Mater.*, 2017, **7**, 1601616.

30 W. Hu, Y. Liu, R. L. Withers, T. J. Frankcombe, L. Norén, A. Snashall, M. Kitchin, P. Smith, B. Gong, H. Chen, J. Schiemer, F. Brink and J. Wong-Leung, *Nat. Mater.*, 2013, **12**, 821–826.

31 Y. Xu, T. F. Tay, L. Cui, J. Fan, C. Niu, D. Chen, Z. Guo, C. Sun, X. L. Zhang and R. A. Caruso, *Inorg. Chem.*, 2020, **59**, 17631–17637.

32 Z. Jin, C. Liu, K. Qi and X. Cui, *Sci. Rep.*, 2017, **7**, 39695.

33 N. Subha, M. Mahalakshmi, S. Monika and B. Neppolian, *Int. J. Hydrogen Energy*, 2020, **45**, 7552–7561.

34 G. Díaz, R. Pérez-Hernández, A. Gómez-Cortés, M. Benaissa, R. Mariscal and J. L. G. Fierro, *J. Catal.*, 1999, **187**, 1–14.

35 D. Tahir and S. Tougaard, *J. Phys.: Condens. Matter*, 2012, **24**, 175002.

36 X. Li, J. Xie, H. Rao, C. Wang and J. Tang, *Angew. Chem., Int. Ed.*, 2020, **59**, 19702–19707.

37 H. Liu, D. Yang, Z. Zheng, X. Ke, E. Waclawik, H. Zhu and R. L. Frost, *J. Raman Spectrosc.*, 2010, **41**, 1331–1337.

38 C. Y. Xu, P. X. Zhang and L. Yan, *J. Raman Spectrosc.*, 2001, **32**, 862–865.

39 W.-T. Chen, V. Jovic, D. Sun-Waterhouse, H. Idriss and G. I. N. Waterhouse, *Int. J. Hydrogen Energy*, 2013, **38**, 15036–15048.

40 X. Qiu, M. Miyauchi, K. Sunada, M. Minoshima, M. Liu, Y. Lu, D. Li, Y. Shimodaira, Y. Hosogi, Y. Kuroda and K. Hashimoto, *ACS Nano*, 2012, **6**, 1609–1618.

41 J. Yu and J. Ran, *Energy Environ. Sci.*, 2011, **4**, 1364–1371.

42 J. Liu, C. Han, X. Yang, G. Gao, Q. Shi, M. Tong, X. Liang and C. Li, *J. Catal.*, 2016, **333**, 162–170.

43 H. Li, C. Tsai, A. L. Koh, L. Cai, A. W. Contryman, A. H. Fragapane, J. Zhao, H. S. Han, H. C. Manoharan, F. Abild-Pedersen, J. K. Nørskov and X. Zheng, *Nat. Mater.*, 2016, **15**, 48–53.

44 D. Wang, Z.-P. Liu and W.-M. Yang, *ACS Catal.*, 2018, **8**, 7270–7278.

45 B. H. R. Suryanto, Y. Wang, R. K. Hocking, W. Adamson and C. Zhao, *Nat. Commun.*, 2019, **10**, 5599.

46 A. K. Mishra, A. Roldan and N. H. de Leeuw, *J. Phys. Chem. C*, 2016, **120**, 2198–2214.